Internal conversion and summing effects in heavy-nuclei spectroscopy

Ch. Theisen, A. Lopez-Martens, Christiane Bonnelle

Internal conversion and summing effects in heavy-nuclei spectroscopy

Ch. Theisen [a,*] A. Lopez-Martens [b] Ch. Bonnelle [c]

[a] *CEA-Saclay, IRFU/Service de Physique Nucléaire, 91191 Gif-sur-Yvette, France*

[b] *CSNSM, IN2P3-CNRS, bat 104-108, 91405 Orsay, France*

[c] *Laboratoire de Chimie Physique - Matière et Rayonnement, Université Pierre et Marie Curie 6, UMR-CNRS 7614, 75231 Paris Cedex 05, France*

Abstract

Internal conversion of low-energy nuclear transitions occurs with a high probability in heavy nuclei. After the emission of the conversion electron, a cascade of X-rays, Auger or Coster-Krönig electrons takes place. In α-decay experiments in which the nuclei of interest are implanted into a silicon detector, these atomic processes contribute to the detected energy. To understand the distortions of the alpha-particle energy spectra, knowledge of the various atomic yields is required. Using state-of-the-art calculations, new atomic yields are computed in $_{99}$Es and compared to those available in the literature. Detailed simulations of the $^{251}_{101}$Md alpha decay are performed and compared to experimental data. Possible ways to discriminate between the available atomic yields are also discussed.

Key words: Internal conversion and extranuclear effects, Fluorescence, Auger effect, α decay.
PACS: 23.20.Nx, 32.50.+d, 32.80.Hd, 23.60.+e

1 Introduction

Internal conversion is an electromagnetic decay process, which competes with γ-ray emission. In the internal conversion process, an excited nucleus interacts with an inner-shell electron causing the electron to be emitted from the atom. The probability of electron emission relative to γ emission increases with the

* Corresponding author.
Email address: christophe.theisen@cea.fr (Ch. Theisen).

atomic number Z of the nucleus and decreases rapidly with increasing transition energy. In heavy-Z nuclei, internal conversion is therefore the dominant process for low-energy nuclear transitions.
Although the measurement of conversion electrons is extremely revealing of the underlying structure of the nucleus, the emission of internal conversion electrons has well-known drawbacks in the case of α-decay spectroscopy after implantation. Indeed, if the α-decay is immediately followed by internal conversion in the daughter nucleus, the energy released in the internal conversion process perturbs the measurement of the α-particle energy. This can lead to an under- or over-estimation of α-decay hindrance factors and may ultimately lead to misinterpretations of the quantum structure of the nuclei of interest.

In this paper, we report on a recent study of the effects of internal conversion on the α-decay spectra of heavy nuclei produced in fusion-evaporation reactions and implanted into a silicon detector at the focal plane of a recoil separator. After recalling the atomic phenomena, which accompany the internal conversion process and reviewing the available atomic data for heavy nuclei, results of new state-of-the-art calculations of atomic yields are presented for the case of the Es element (Z=99). In the last part of the paper, detailed Geant4 simulations of the α-decay of ^{251}Md and subsequent electromagnetic decay of ^{247}Es are performed and compared to experimental data.

2 Atomic phenomena following internal conversion

In the internal conversion process, the energy, E_γ, of a transition between two nuclear states is carried away by an atomic electron. If BE_i is the binding energy of the atomic electron shell, i, and small recoiling effects are neglected, the energy of the conversion electron is given by:

$$E_e = E_\gamma - BE_i. \tag{1}$$

The actual atomic shell (K, $L1$, $L2$, $L3$, $M1$,...,$M5$,...) from which the conversion electron originates is determined by the properties of the nuclear transition, namely its energy and electric or magnetic multipole. For example the conversion of a magnetic dipole transition will not lead to the same distribution of conversion electrons from the L-shell as the internal conversion of an electric quadrupole transition.

The internal conversion process leaves the atom with a vacancy in one of its inner shells. The ionized atom relaxes and loses some its energy in two ways: X-ray fluorescence or electron emission.
As is illustrated in Fig. 1a), when a vacancy in the $L1$ sub-shell is filled by a $M2$ electron, a characteristic X-ray can be emitted. The energy of the emitted radiation is the difference between the binding energies of the atomic shells involved in the process:

$$E_{XL1-M2} = BE_{L1} - BE_{M2}. \tag{2}$$

After the X-ray emission, the atom is left with a secondary vacancy in the $M2$ sub-shell.
Emission of an Auger electron is an alternative to the emission of an X-ray. Taking again the example of an internal conversion on the $L1$ sub-shell, the energy released in the filling of the $L1$ vacancy by an $M2$ electron can be transferred to an $M3$ electron, which escapes from the atom. This is shown in Fig. 1b). In this case, the energy of the Auger electron is given in a first approximation by:

$$E_{AL1-M2M3} = BE_{L1} - BE_{M2} - BE_{M3}. \tag{3}$$

The atom is then left with two secondary vacancies, one in the $M2$ sub-shell and another in the $M3$ sub-shell.
A special case of Auger transition occurs when the vacancy is filled by an electron from a higher subshell of the same shell. This process, called a Coster-Krönig transition, is presented in Fig. 1c). The vacancy in $L1$ is filled by an $L3$ electron causing an $M2$ electron to be ejected from the atom with the energy:

$$E_{AL1-L3M2} = BE_{L1} - BE_{L3} - BE_{M2}. \tag{4}$$

There are also rearrangement phenomena where there is a mixing between photon emission and Auger electron emission. The energy is shared between the two particles and the resulting photons have lower energies than characteristic X-ray photons. This phenomenon is called the radiative Auger effect but its probability, largest for low-Z elements, is very small.
In all the cases, the secondary vacancies will be, in turn, filled by other electrons. Continuation of these processes gives rise to an atom with multiple vacancies in its outermost shells.

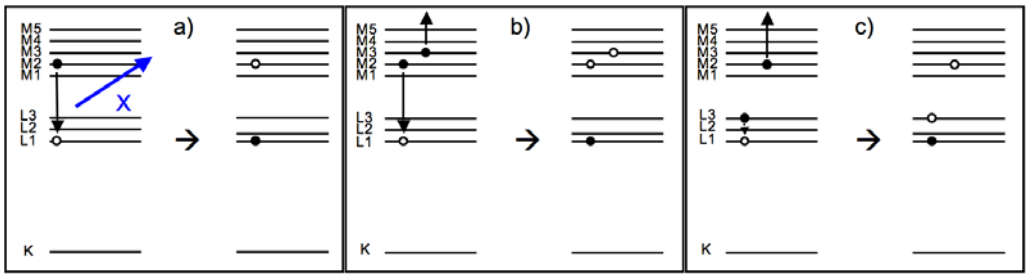

Fig. 1. Schematic illustration of how the filling of a primary vacancy in the $L1$ atomic sub-shell can produce a) X-ray fluorescence b) the emission of an Auger electron and c) a Coster-Krönig transition. The resulting secondary vacancies are shown in each case.

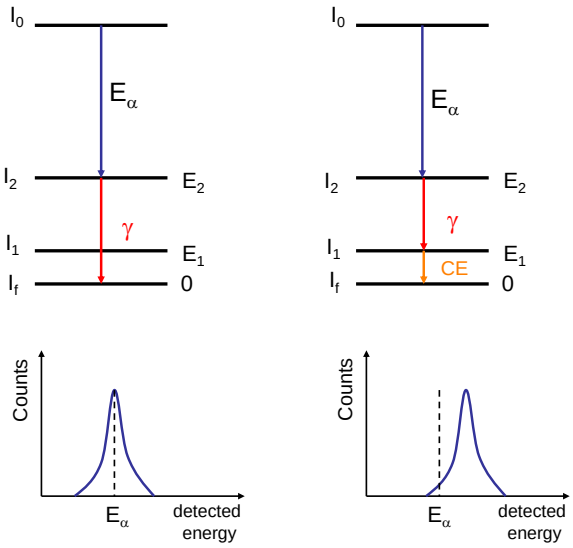

Fig. 2. [color online] Schematic example of how coincident alpha decay and internal conversion leads to an apparent alpha-particle energy higher than its true energy E_α. See text for details.

2.2 Summing effect

Summing occurs when an alpha transition is in prompt coincidence with an internally converted nuclear transition . The energy deposited by the α particle sums up with the energy of the conversion electron and subsequent X-rays, Auger and Coster-Krönig electrons. A typical example is shown in Fig. 2. An α transition feeds the I_2 state, which decays via two parallel branches. The first branch $I_2 \rightarrow I_f$ is assumed radiative with no energy deposited in the silicon detector, the energy detected being E_α. The second branch consists of a radiative transition $I_2 \rightarrow I_1$ (with no energy deposition in the silicon detector) in coincidence with a converted transition $I_1 \rightarrow I_f$, whose energy sums up with the alpha particle energy. The energy detected in the silicon detector is

therefore larger than E_α, leading to a satellite peak on the right of the "true" alpha line. In typical experiments, however, recoil nuclei are implanted near the surface of a thin silicon detector. Part of the X-rays, Auger and Coster-Krönig electrons energy can escape from the detector, thereby depositing only a fraction of their energy. The energy detected in the silicon detector does therefore not necessarily correspond to the sum of the energies of the α line and coincident converted transition. The apparent energy distribution of the alpha line in coincidence with the converted transition depends on the ranges in silicon of the emitted X-rays and/or electrons, hence on their energies, on the relative yields of radiative and non-radiative emission and on the actual implantation depth of the recoils.

2.3 Atomic yields

In order to qualify and quantify the energy release at each step of the sequence of vacancy fillings after the internal conversion process, it is necessary to know the yields of the different competing processes.

The atomic yields for a vacancy in the K and L shells of elements up to Z =110 (Darmstadtium) have been evaluated by Krause [1] on the basis of experimental and theoretical information. K-fluorescence yields, ω_K, are small below Z=20 but increase rapidly with Z. For the heaviest nuclei, practically every vacancy in the K-shell is followed by X-ray emission. L-fluorescence yields, ω_L, are smaller than K-fluorescence yields but also increase with Z. For Z=99 (Einsteinium), the fluorescence yield are close to 50% for a vacancy in the $L2$ or $L3$ sub-shells. Although Coster-Krönig transitions do not release much energy, their yield f is far from being negligible and has a large impact on the total L-fluorescence yield since for example, more than 50% of the $L1$ vacancies in Einsteinium result in a $L3$ vacancy.

For most initial and final shell vacancies, K and LX-ray intensities can be found in the Table of Isotopes [2]. They are determined from the atomic yields of Krause and from experimental (and sometimes theoretical) relative emission probabilities. For LX-rays, the intensities account for primary and secondary shell vacancies, i.e. they account for intra-shell radiative processes as well as intra- and inter-shell non-radiative processes.

The lack of experimental data and detailed theoretical calculations for heavy elements (Z >93) is a source of large uncertainties. Indeed, the estimated uncertainties in the fluorescence yields can be as large as 20%. Coster-Krönig yields for vacancies in the $L1$ shell are even more uncertain.

In order to check the reliability of the tabulated atomic yields, new and accurate calculation of X-ray, Auger and Coster-Krönig yields for the L shell were performed in the case of Einsteinium (element Z=99).

2.4 Note on the radiative and non-radiative nomenclature

For X-rays, Auger and Coster-Krönig transition, we will use the IUPAC recommendations [3]. The nomenclature for X-rays introduced by Siegbahn in the 1920's is abundantly chosen in evaluations such as the Table of Isotopes [2]. We would like to point-out that the Siegbahn notation considers the most intense X-rays only. Moreover, only the most intense rates are reported in [2], most X-rays considered by Siegbahn being ignored. In order to make comparisons between the new yields reported in this article and those given in [2], we will also quote the Siegbahn notation. For non-radiative transition, we use the standard notation XY-Z, X corresponding to the initial vacancy, Y to the shell filling the vacancy and Z to the shell from which the electron is ejected. For radiative or non-radiative transition involving the same shell, the f'_{12}, f'_{13}, f'_{23}, f_{12}, f_{13}, f_{23} notation is usually used for the $L1$-$L2$, $L1$-$L3$, $L2$-$L3$, $L1$-$L2X$, $L1$-$L3X$, $L2$-$L3X$ transitions, respectively.

2.5 New atomic calculations

Radiative and non-radiative transition rates are computed using a multiconfiguration Dirac-Fock (MCDF) program including the Breit interaction, quantum electrodynamics corrections and nuclear masses. A description of the code on which the new calculations are based can be found in [4]. The Extended Average Level (EAL) procedure allows all initial and final levels to be calculated simultaneously [5]. To correct for first order relaxation effects, which arise from the common description of the initial and final atomic states involved in the transition of interest, the Slater transition state is used [6].
This method has been used to deduce X-ray and Auger electrons energies and relative intensities for a large range of atomic numbers; see [7] for the rare-earth region. K X-ray fluorescence yields have been calculated, as an example, for the free Cu atom. The calculation gives $\omega_K = 45.4\%$ compared to an experimental value of $45.4 \pm 0.9\%$. Results reported here for Es, much heavier than Cu, are expected to be of the same quality since the calculation is relativistic and since the nuclear size is taken into account. Moreover, the code has been developed to predict the atomic properties of heavy elements such as U and Pu.
All possible transitions are calculated: electric dipole and quadrupole radiative transitions as well as all energetically allowed non-radiative transitions. Radiative magnetic transitions are not included since their rates are negligible. Description of a neutral atom involving the f^{10} sub-shell introduces a level of complexity preventing the calculation of non-radiative transitions (see for instance [7]). Therefore, calculations are made using the f^0 multi-charged ion configuration. The consistency of this approximation has been checked. The

yield uncertainties are estimated to be a few %.
Tables 1, 2 and 3 resume the results of radiative calculations and compares them to the values tabulated in the Table of Isotopes [2]. Non radiative yields are given in table 4. We would like to point-out a discrepancy in the $L1$ fluorescence yields given in Ref. [2], which has been confirmed by the authors [8]. In this compilation, it has been assumed that the intra-shell radiative yield f'_{13} is negligible compared to ω_{L1}. Therefore the sum of the yields for the transitions $L1$-$M2$ ($L_{\beta 4}$), $L1$-$M3$ ($L_{\beta 3}$), $L1$-$N2$ ($L_{\gamma 2}$) and $L1$-$N3$ ($L_{\gamma 3}$) is equal to ω_{L1} while the correct value is $\omega_{L1} - f'_{13}$ (neglecting f'_{12} and other X-ray transitions having an intensity less than 1%). In table 1, the intensities of the $L1$-$M2$, $L1$-$M3$, $L1$-$N2$ and $L1$-$N3$ X-rays from Ref. [2] have therefore been scaled by a factor $(\omega_{L1} - f'_{13})/\omega_{L1}$.

Table 1: X-ray energies and intensities per 100 $L1$ primary vacancies as a function of initial and final shell vacancies for Einsteinium. Rate and intensity uncertainties from this work are estimated at a few %.

X-ray		Energy (keV, this work)	Rate 10^{15} s^{-1} (this work)	Intensity (this work)	Intensity ([2])
$L1$-$L2$	(f'_{12})	0.9	0.0004	0.0001	-
$L1$-$L3$	(f'_{13})	6.4	0.4522	1.74	2.1
$L1$-$M2$	($L_{\beta 4}$)	20.2	1.9463	7.47	9.2 (16)
$L1$-$M3$	($L_{\beta 3}$)	21.5	1.37	5.26	6.7 (12)
$L1$-$N2$	($L_{\gamma 2}$)	25.1	0.5456	2.09	4.1 (7)
$L1$-$N3$	($L_{\gamma 3}$)	25.4	0.4666	1.79	3.1 (5)
$L1$-$O2$	($L_{\gamma 4'}$)	26.4	0.1478	0.57	-
$L1$-$O3$	($L_{\gamma 4}$)	26.5	0.1329	0.51	-
$L1$-$P2$	($L_{\gamma 13}$)	26.8	0.0462	0.18	-
$L1$-$P3$	($L_{\gamma 13}$)	26.8	0.0428	0.16	-
$L1$-$M4$	($L_{\beta 10}$)	22.1	0.1058	0.41	-
$L1$-$M5$	($L_{\beta 9}$)	22.4	0.1566	0.6	-
$L1$-$N4$		25.7	0.0198	0.08	-
$L1$-$N5$	($L_{\gamma 11}$)	25.8	0.0319	0.12	-
$L1$-$O4$		26.7	0.0044	0.02	-

Table 1: continued

X-ray	Energy (keV, this work)	Rate 10^{15} s^{-1} (this work)	Intensity (this work)	Intensity ([2])
$L1$-$O5$	26.7	0.0072	0.02	-

Table 2: Same as table 1 for $L2$ primary vacancies.

X-ray	Energy (keV, this work)	Rate 10^{15} s^{-1} (this work)	Intensity (this work)	Intensity ([2])
$L2$-$M4$ $(L_{\beta 1})$	21.2	6.9798	39.32	37 (4)
$L2$-$N4$ $(L_{\gamma 1})$	24.8	1.73942	9.80	9.5 (10)
$L2$-$O4$ $(L_{\gamma 6})$	25.7	0.43273	2.44	2.0 (3)
$L2$-$M1$ (L_{η})	18.9	0.20593	1.16	1.04 (11)
$L2$-$N1$	23.9	0.05796	0.33	-
$L2$-$O1$	25.4	0.01642	0.09	-
$L2$-$P1$	25.8	0.00527	0.03	-
$L2$-$M23$	20.6	0.01096	0.06	-
$L2$-$N23$	24.5	0.00356	0.02	-
$L2$-$O23$	25.6	0.001	0.006	-
$L2$-$P23$	25.9	0.00032	0.001	-

Table 3: Same as table 1 for $L3$ primary vacancies.

X-ray	Energy (keV, this work)	Rate 10^{15} s^{-1} (this work)	Intensity (this work)	Intensity ([2])
$L3$-$M4$ $(L_{\alpha 2})$	15.7	0.57292	3.84	4.11 (18)
$L3$-$M5$ $(L_{\alpha 1})$	16.0	5.02655	33.7	36.7 (16)
$L3$-$N4$ $(L_{\beta 15})$	19.4	0.12382	0.83	10.5 (5)

Table 3: continued

X-ray	Energy (keV, this work)	Rate 10^{15} s^{-1} (this work)	Intensity (this work)	Intensity ([2])
$L3$-$N5$ ($L_{\beta 2}$)	19.4	1.14450	7.7	
$L3$-$O4$ ($L_{\beta 5}$)	20.2	0.0298	0.20	2.41 (11)
$L3$-$O5$ ($L_{\beta 5}$)	20.2	0.2792	1.87	
$L3$-$M1$ (L_l)	13.4	0.3903	2.62	2.9 (3)
$L3$-$N1$ ($L_{\beta 6}$)	18.5	0.1017	0.68	0.78 (4)
$L3$-$O1$ ($L_{\beta 7}$)	19.9	0.0283	0.19	-
$L3$-$P1$	20.4	0.0091	0.06	-
$L3$-$M2$ (L_t)	13.8	0.0047	0.03	-
$L3$-$N2$	18.7	0.0010	0.07	-
$L3$-$O2$	20.0	0.0002	0.01	-
$L3$-$P2$	20.4	0.0001	0.007	-

Table 4: Auger and Coster-Krönig intensities per 100 primary vacancies for Einsteinium. Rate and intensity uncertainties are estimated at a few %.

Transition	Rate 10^{15} s^{-1} (this work)	Intensity (this work)
$L1$-$L2X$ (f_{12})	1.0767	4.13
$L1$-$L3X$ (f_{13})	16.0825	61.7
$L1$-$M1X$	1.8121	6.95
$L1$-$M2X$	0.2879	1.10
$L1$-$M3X$	0.1457	0.56
$L1$-$M4X$	0.6144	2.36
$L1$-$M5X$	0.3906	1.50
$L1$-$N1X$	0.08749	0.34
$L1$-$N2X$	0.01656	0.06

Table 4: continued

Transition	Rate 10^{15} s^{-1} (this work)	Intensity (this work)
$L1$-$N3X$	0.01090	0.04
$L1$-$N4X$	0.02719	0.10
$L1$-$N5X$	0.01960	0.07
$L1$-$N6X$	0.00217	0.008
$L1$-$N7X$	0.00202	0.008
$L1$-OX	0.0085	0.03
$L1$-PX	0.0003	0.0012
$L2$-$L3X$ (f_{23})	3.68331	20.75
$L2$-$M1X$	0.33689	1.90
$L2$-$M2X$	1.80474	10.2
$L2$-$M3X$	0.52176	2.94
$L2$-$M4X$	1.42407	8.0
$L2$-$M5X$	0.28522	1.6
$L2$-$N1X$	0.01978	0.11
$L2$-$N2X$	0.08912	0.50
$L2$-$N3X$	0.03065	0.17
$L2$-$N4X$	0.06814	0.38
$L2$-$N5X$	0.01799	0.10
$L2$-$N6X$	0.00184	0.01
$L2$-$N7X$	0.00148	0.08
$L2$-OX	0.01176	0.07
$L2$-PX	0.00037	0.002
$L3$-$M1X$	0.43273	2.90
$L3$-$M2X$	0.66928	4.49
$L3$-$M3X$	2.18774	14.67
$L3$-$M4X$	1.62247	10.88
$L3$-$M5X$	1.89422	12.70

Table 4: continued

Transition	Rate 10^{15} s^{-1} (this work)	Intensity (this work)
$L3$-$N1X$	0.02207	0.15
$L3$-$N2X$	0.03345	0.22
$L3$-$N3X$	0.09588	0.64
$L3$-$N4X$	0.07984	0.54
$L3$-$N5X$	0.12493	0.84
$L3$-$N6X$	0.00532	0.04
$L3$-$N7X$	0.00479	0.03
$L3$-OX	0.01451	0.010
$L3$-PX	0.00035	0.002

Fluorescence yields are summarized in table 5. What is immediately noticeable from table 5 is the smaller $L1$ and $L3$ X-ray yields, ω_{L1} and ω_{L3}. However, the calculated Coster-Krönig transition rates are generally larger, especially f_{13}, and this will affect the total X-ray rates. The $L2$ X-ray rate after a $L1$ vacancy is given by:

$$X_{L2} = (f_{12} + f'_{12}) \times \omega_{L2}. \tag{5}$$

Similarly, the $L3$ X-ray rate following a $L1$ vacancy is:

$$X_{L3} = (f_{12} \times f_{23} + f_{13} + f'_{13}) \times \omega_{L3}, \tag{6}$$

where f'_{12} and f'_{13} are the inner-shell radiative yields ($f'_{12} << f'_{13}$). The effective fluorescence yields ν_1 and ν_2 correspond to the total X-ray yield after an initial vacancy in the $L1$, $L2$ shell respectively and are given by:

$$\nu_1 = \omega_{L1} + (f_{12} + f'_{12}) \times \omega_{L2} + (f_{12} \times f_{23} + f_{13} + f'_{13}) \times \omega_{L3}, \tag{7}$$

$$\nu_2 = \omega_{L2} + f_{23} \times \omega_{L3}. \tag{8}$$

The effective yields ν_1 and ν_2 are found to be 55.5 and 64.0 respectively, compared to 59.1 and 60.9 in [1] (see tables 6 and 7). Although the numbers may be similar, the distributions of X-ray energies differ slightly.

Table 5
Comparison between the calculated transition rates and the transition rates of [1]. First 3 lines: Fluorescence yields per vacancy in the $L1$, $L2$ and $L3$ sub-shells. Next two lines: Coster-Krönig yields per vacancy in the $L1$ sub-shell leading to a vacancy in the $L2$ and $L3$ sub-shells (f_{12} and f_{23}). Next line: intra-shell radiative yield per vacancy in the $L1$ sub-shell leading to a vacancy in the $L3$ sub-shell (f'_{13}). Last line: Coster-Krönig yield per vacancy in the $L2$ shell resulting in a vacancy in the $L3$ sub-shell (f_{23}).

Yield (in %)	This work	[1]
ω_{L1}	21.0	25.3
ω_{L2}	53.3	49.7
ω_{L3}	51.8	57.0
f_{12}	4.1	3
f_{13}	61.7	54
f'_{13}	1.74	2.1
f_{23}	20.7	19.6

Table 6
First 3 lines: $L1$, $L2$ and $L3$ effective fluorescence yield after $L1$ vacancy. Last line: total effective yield after $L1$ vacancy.

Yield (in %)	This work	[1]
$L1$	21.0	25.3
$L12$	2.2	1.5
$L13$	32.3	32.3
ν_1	55.5	59.1

Table 7
First 2 lines: $L2$ and $L3$ effective fluorescence yield after $L2$ vacancy. Last line: total effective yield after $L2$ vacancy.

Yield (in %)	This work	[1]
$L2$	53.3	49.7
$L23$	10.7	11.2
ν_2	64.0	60.9

3 Geant4 Simulations

In this section, we compare experimental results on the decay of $^{251}_{101}$Md to its daughter $^{247}_{99}$Es with Geant4 simulations. The details of the analysis and

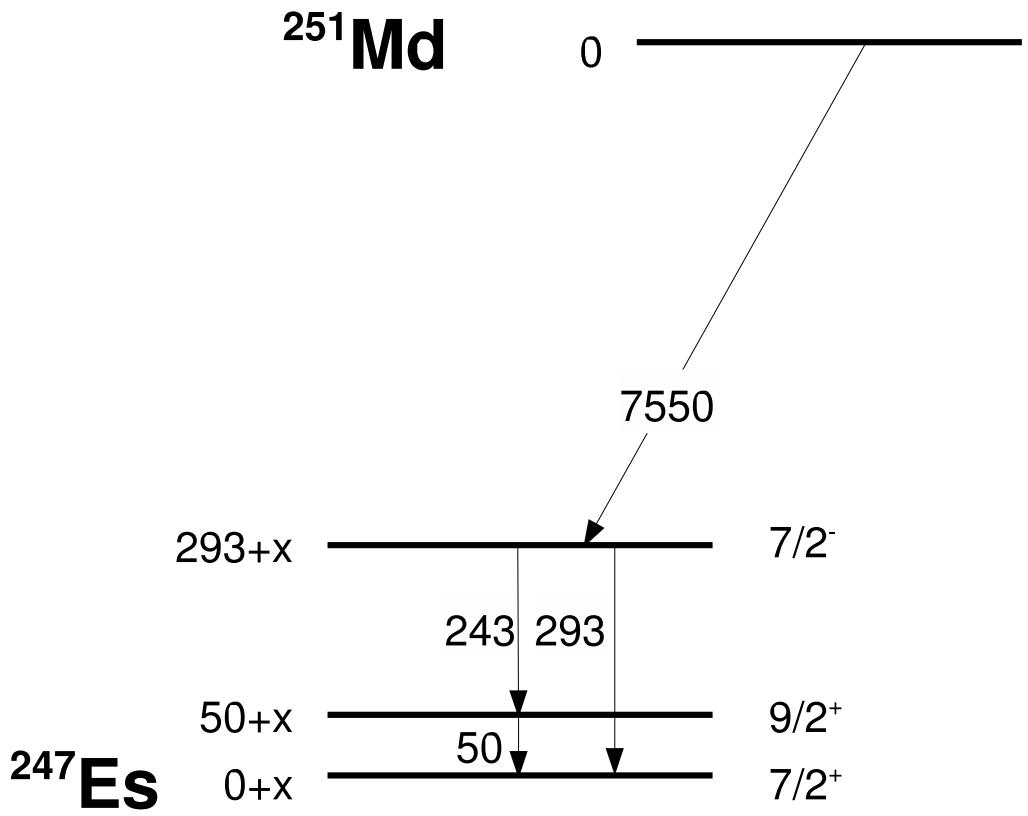

Fig. 3. Decay scheme of $^{251}_{101}$Md taken from [9].

interpretation of the data are reported in [9]. The decay scheme of $^{251}_{101}$Md is shown in Fig. 3. As explained in [9], both transition at 243 and 293 keV are deduced to be electric dipole $E1$, while the 50 keV transition is a magnetic dipole $M1$.

3.1 Experimental set-up

Although the experimental setup has been described in [9], we will briefly recall the aspects, which are relevant for performing the simulations and comparing them to the experimental data.
The detection setup was installed at the focal plane of the LISE spectrometer [10] in GANIL. It consists of an array of silicon detectors called BEST (Box for Electron Spectroscopy after Tagging) surrounded by a set of four germanium clover detectors from the EXOGAM collaboration [11], placed as close as possible to the silicon detectors. A photography of BEST, for which the upper part of the vacuum chamber has been removed, is shown in Fig. 4. BEST is situated downstream from a start detector, which comprises one emissive foil (0.9 μm mylar) tilted at 45° with respect to the beam axis and coupled to a multichannel plate. The evaporation residues ^{255}Lr produced in the fusion-

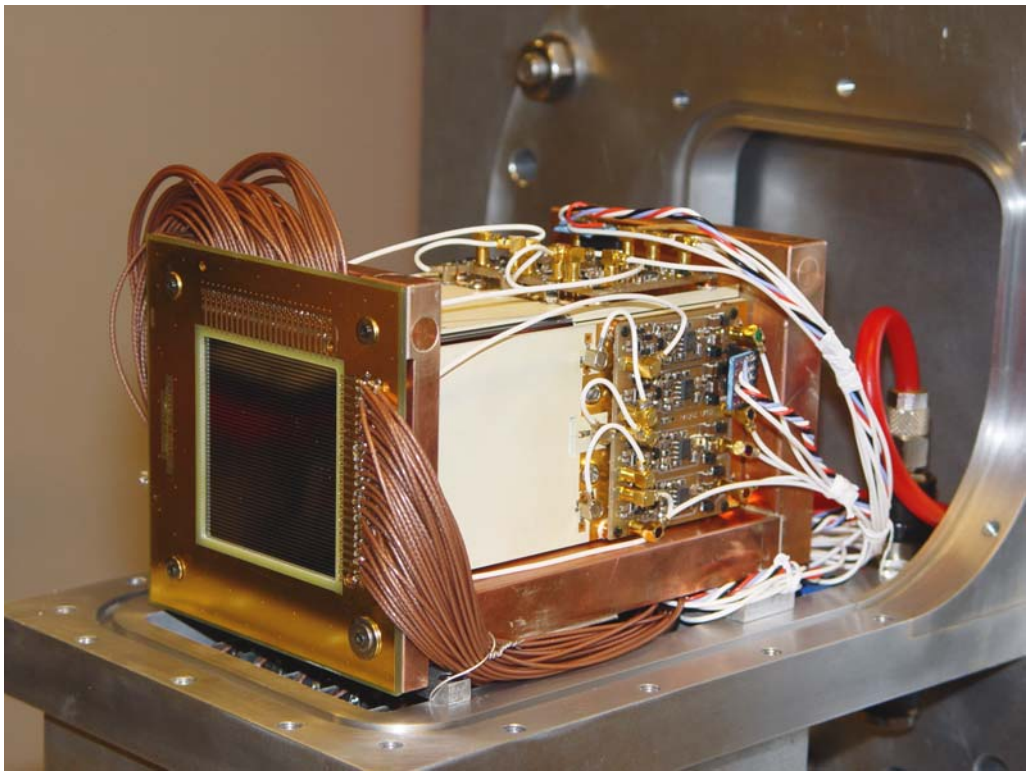

Fig. 4. [color online] Picture of the BEST array.

evaporation reaction ^{209}Bi(^{48}Ca,2n)^{255}Lr arrive from the right of Fig. 4 and are implanted at a few microns depth into a 300 μm-thick Double Sided Silicon Detector (DSSD). The 50×50 mm^2 detector has 48 strips on each side. All 96 strips are instrumented with charge preamplifiers designed at GANIL, which are mounted beneath the vacuum chamber. The Time of Flight (ToF) is measured between the start detector and the DSSD. After implantation, the ^{255}Lr evaporation residue decays via two successive α emissions to its granddaughter ^{247}Es.

Four 50×50 mm^2 1 mm-thick silicon detectors are positioned in a tunnel-like configuration upstream from the implantation detector. This tunnel is used to detect internal conversion electrons and α particles escaping from the implantation detector. The silicon detectors have thin 0.15 μm aluminum windows to minimize energy losses of the conversion-electrons and are segmented into four squares to minimize the capacitance and therefore optimize the electron energy resolution. Each tunnel detector is mounted on a ceramic board, which also carries a four-channel charge preamplifier designed at GANIL.

The PCB's of the five silicon detectors are supported by a copper frame in which a cooling liquid at a temperature of -15°C circulates. The gap between the active part of the silicon tunnel detectors and the implantation detector is 15 mm. The resolution of the implantation detector is measured to be $\sim$ 40 keV for the α lines of a mixed ^{239}Pu, ^{241}Am and ^{244}Cm source. The resolution of the tunnel detector is $\sim$ 8 keV for the $K365$ electron line of a ^{133}Ba

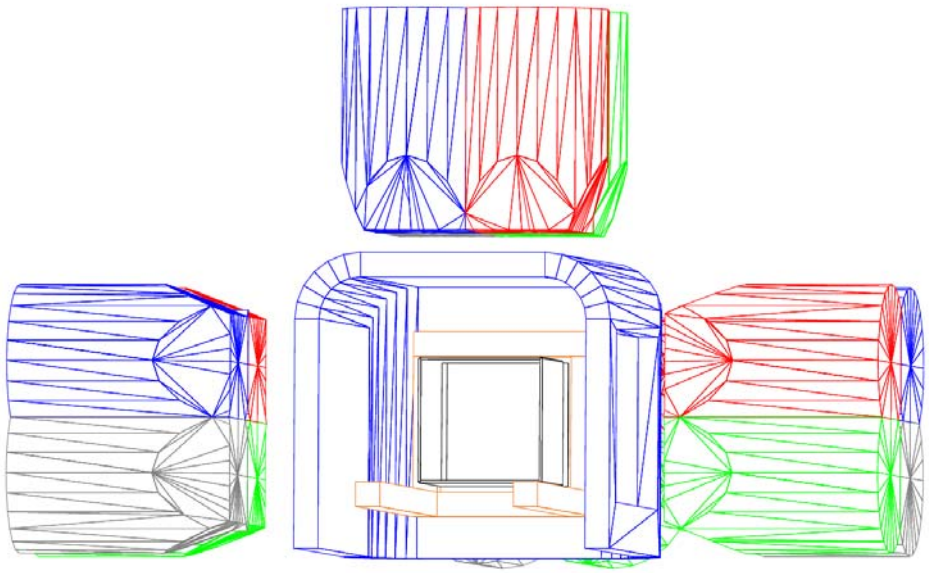

Fig. 5. [color online] BEST geometry defined in the Geant4 package, as seen from the incoming recoil nuclei.

source, and <20 keV for the α lines of the mixed source. These resolutions are obtained for a fluid temperature of -15°C. The detector gains are periodically checked using the mixed and ^{133}Ba sources, which can be inserted into the vacuum chamber at the entrance of the tunnel. The sources are first moved down into the beam axis and then moved near the tunnel using a mechanism based on a camera zoom lens. During in-beam measurements, the silicon detectors are shielded from the sources.
The walls of the vacuum chamber are reduced to 1.5 mm in front of the germanium detectors to minimize the γ-ray absorption at low energy.
For comparison, we will also show and discuss results obtained at the University of Jyväskylä using the GREAT [12] array and at Dubna with the GABRIELA focal plane setup [13].

3.2 Simulation procedure

Simulations were performed with the Geant4 package [14]. A picture of the geometry of the setup described with the Geant4 code is shown in Fig. 5. Some parts of the setup are not shown for more visibility: the ceramics plates on which the silicon tunnel detectors are mounted, part of the copper frame and the aluminum caps of the germanium detectors.
The physics input corresponds to the level scheme shown in Fig. 3: the emission of a 7550 keV alpha-particle is promptly followed either by the emission of a 293 keV γ-ray or associated conversion electron or by a 2-step cascade

consisting of a 243 keV γ-ray or conversion electron and 50 keV γ-ray or associated conversion electron. The branching ratio for the 1-step cascade is given by the experiment: 87% [9]. Conversion coefficients for the two $E1$ transitions and the $M1$ transition are taken from [15]. Note that in the similar simulations presented in [9], the γ-emission or internal conversion of the 243 and 293 keV transitions were not included.

The position of the vertex corresponding to the α and subsequent γ and/or electron emissions is randomly chosen in the implantation detector with a x-y distribution corresponding to the experimental one (the z direction being parallel to the beam axis). Using this implantation profile, the clover array and electron tunnel efficiencies were simulated (see Fig. 6). The total γ-ray efficiency peaks at $\sim$23% for photon energies of 100 keV. About half of the detection efficiency is accounted for by the clover detector facing the implantation detector. The electron detection efficiency is rather flat as a function of energy and is $\sim$8% for an implantation depth of 5 μm. This is half of the plateau efficiency of the tunnel of GABRIELA [13], which is of similar design. This difference is due to the smaller gap between the tunnel silicon detectors and the implantation detector ($\sim$ 2.5 mm *vs* 15 mm). Absolute electron efficiency measurements performed in-beam with GABRIELA are well reproduced by Geant4 simulations [13] and support the present simulated performances of BEST.

When internal conversion occurs, X-rays, Auger or Coster-Krönig electrons are generated according to the yields from [2] or from this work. The vacancy is then propagated and subsequent atomic processes are generated. When the process reaches the M shell or a higher one, the available energy is less than the M shell binding energy in Einsteinium, i.e. less than 7 keV. Since the M shell fluorescence yield ω_M is about 8% [16], only electron emission is assumed. The particles emitted in the subsequent vacancy fillings will therefore not have enough energy to escape from the implantation detector. As an example, the range of 10 keV electrons in silicon is about 1.5 μm. This is why we approximate the remaining relaxation processes by the emission of a single electron having the available remaining energy.

Since a DSSD has been used, the effect of the segmentation on potential energy sharing between strips has been investigated. The simulations show that this effect is negligible: the energy deposited in the neighbouring strips is small and bellow the detection threshold.

The spectral distortion arising from the shake-off process, in which the atom is ionized during α decay (see for instance [17]), has also been investigated. The associated α-particle energy spectrum peaks at an energy which is equal to the original α-particle energy minus the binding energy of the electron. In ^{210}Po, the probability of electron shake-off from the K, L and M shells is found to be $\sim 10^{-6}$, 10^{-4} and 10^{-3} respectively [18,19]. Given the statistics obtained in the experiments and the uncertainties in atomic yields and internal conversion coefficients, the shake-off process involving the K or L shells can be ignored. The process becomes significant for the most outer shells but since the ener-

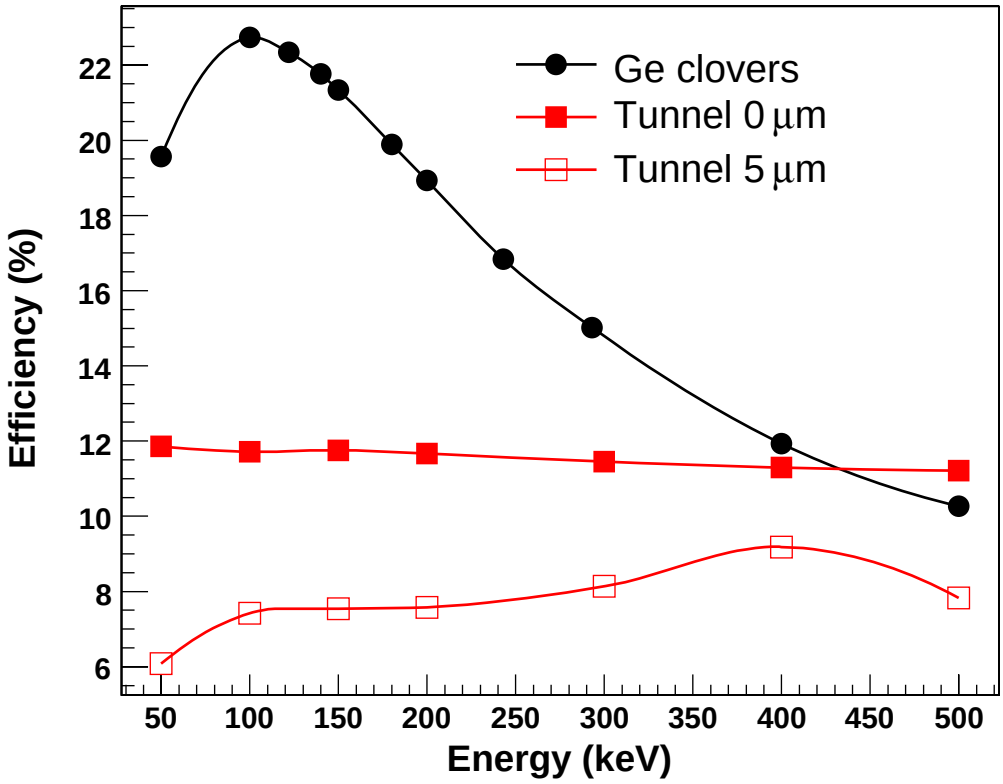

Fig. 6. [color online] Efficiency of the BEST array simulated with Geant4. The tunnel electron efficiency is simulated for recoil implantation depths of 0 and 5 μm. The procedure to extract the electron efficiency is the same as in Ref. [13].

gies of the α-particle and electron will sum up in the implantation detector, the effective α-particle energy remains unchanged. This is why the electron shake-off accompanying α decay has not been considered.

3.3 Results

Stopping powers are not well known in the heavy element mass region and only extrapolations can be used. We have used the LISE++ [20] and SRIM-2006 [21] codes to estimate energy losses and implantation depths of the recoiling ^{255}Lr nuclei. The LISE++ code uses energy losses from [22] and ranges from [23]. Since the SRIM-2006 code does not allow calculation above uranium, we have assumed U nuclei with the same energy per nucleon as ^{255}Lr recoil nuclei. Both codes lead to a ^{255}Lr recoil nuclei of average kinetic energy 31 MeV after emerging from the middle of the target and passing through the start detector. In both cases, an implantation depth of 5 μm in the DSSD is obtained. In the simulations, no DSSD entrance window or dead layers have been assumed.
Results of the simulations using the yields from [2] and from this work are

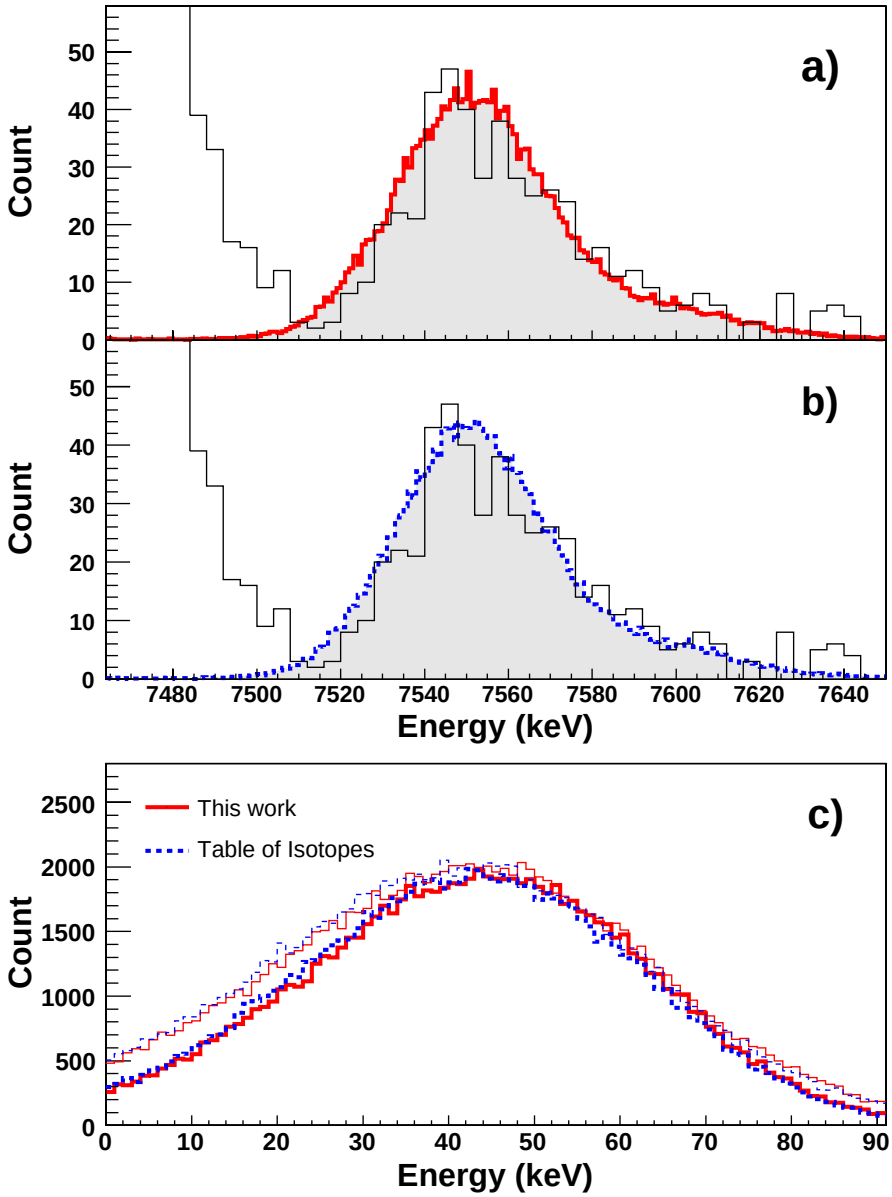

Fig. 7. [color online] Experimental spectrum (thin line) of energies detected in the DSSD of BEST compared to a) the simulated spectrum obtained with the atomic yields of this work (thick line) and b) the simulated spectrum obtained with atomic yields from [2] (thick dashed line). c) simulated energy deposited in the implantation detector following the internal conversion of the 50 keV (thick line: yields from this work, thick dashed line: yields from [2]) and for the 50, 243 and 293 keV transitions (thin line: yields from this work, thin dashed line: yields from [2]).

shown in Fig. 7. Figures 7a) (yields from this work) and 7b) (yields from [2]) compare the simulated energy spectra obtained in the implantation detector with the experimental data. Simulations are folded with the experimental detector resolution which is of 40 keV with BEST. From these two figures, it

appears that both simulations reproduce the experimental data well and that no major differences due to different atomic yields are visible.
Figure 7c) shows the simulated energy deposited in the implantation detector without the contribution of the 7500 keV α transition. The thick lines correspond to simulations for which only the contribution of the 50 keV transition is computed. Experimentally, such a contribution can be obtained by gating on the 243 keV radiative transition. The average energy deposited in the silicon detector is 41.8 ± 0.2 keV using the atomic yields from this work and 40.9 ± 0.2 keV using the yields from [2]. Small differences in the shape of the distributions can be observed, but they are not significant. These will be discussed in section 4. The simulated energy deposited in the implantation detector, which results when the contributions of the 50, 243 and 293 keV transitions are included, is shown with thin lines. These spectra display a low energy tail due to the Compton scattering of the 243 and 293 keV γ-rays in the silicon detector. The effect of this tail is to shift the average energy to lower energies. Note that the distribution is not Gaussian; fitting the distribution with a Gaussian underestimates slightly the average energy.
For comparison, we have displayed in Fig. 8 the same type of spectra with data taken at the University of Jyväskylä. In this case, the experimental spectrum results from recoil-α-α correlations and the simulations were performed with an implantation depth of 3 μm, value obtained with the LISE++ and SRIM-2006 codes. Indeed, after passing through the MWPC ToF detector (which corresponds to a total mylar thickness of 320 μg/cm^2 for the entrance and exit windows, and 12 cm of isobutane at 3 mbar) and a degrader foil (100 μg/cm^2 mylar), ^{255}Lr recoils have an average energy of 19 MeV. Note that the energy resolution of the GREAT implantation detector is $\sim$25 keV compared to $\sim$40 keV with BEST. This is why the two components of the alpha distribution at 7550 and 7590 keV can clearly be separated. Again, no significant differences between the experimental data and the simulations are observed: the average energy deposited by the 50 keV transition only is 39.6 ± 0.2 keV using the atomic yields from this work and 38.8 ± 0.2 keV using the yields from [2]. For both atomic yields, the maximum of the distribution is at ~ 50 keV while the average energy is ~ 10 keV lower. This explains why the experimental energy of the summed peak is at 7590 keV while a full absorption of a conversion electron and subsequent X-rays and/or Auger electrons should lead to a peak at 7600 keV. The data taken at the University of Jyväskylä are well reproduced using an implantation depth of 3 μm: the centroid of the distribution is reproduced with an accuracy of about 1 keV. This provides good confidence in the simulations.

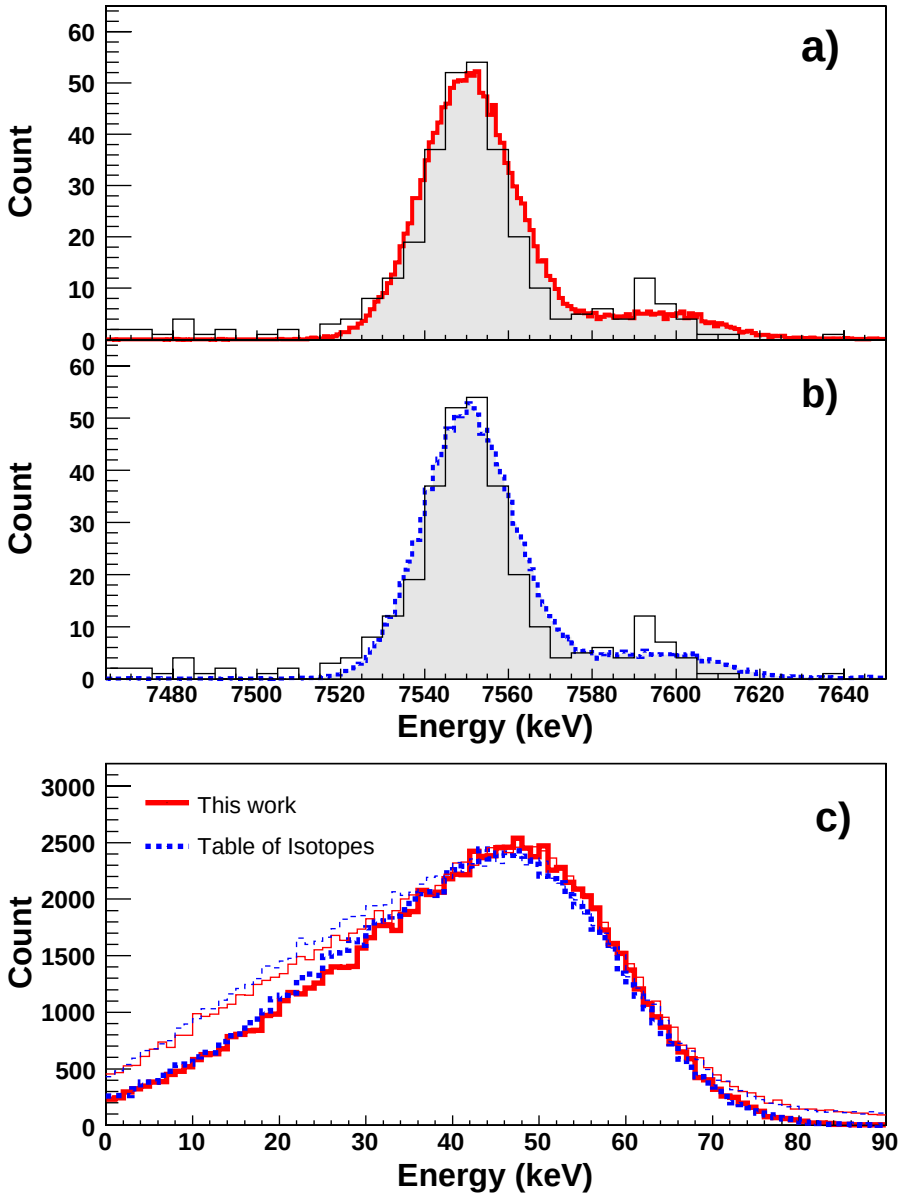

Fig. 8. [color online] Same as Fig. 7 with data taken at the University of Jyväskylä.

4 Discussion

The conversion of the 50 keV $M1$ transition occurs mainly in the $L1$ shell. According to the new atomic yield calculations, a large fraction of the subsequent relaxation processes ($f_{13} = 61.7\%$) follow a Coster-Krönig transition to the $L3$ shell. As a consequence, even though ω_{L1} and ω_{L3} are 17% and 10% smaller than the values tabulated in [1] (cf table 5), the new effective fluorescence yield ν_1 is only slightly smaller (55.5% compared to 59.1%).
Since radiative transitions are only partially measured in the implantation

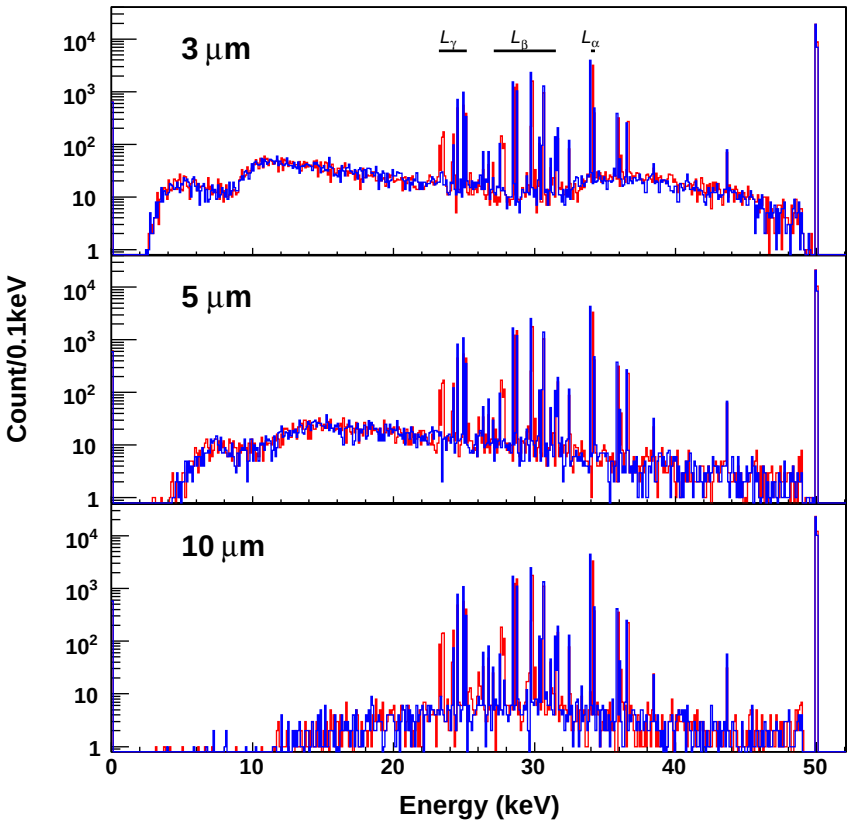

Fig. 9. [color in print] Simulated spectra of the total energy deposited in the implantation detector by the internal conversion process of the 50 keV transition using the atomic yields of this work (red curve) of from [2] (blue curve) for different implantation depths. The energy distributions are not folded with the implantation detector resolution.

detector, one expects more sensitivity to differences in atomic yields at large implantation depths, for which the probability of electron escape is smaller. Obviously, the sensitivity also depends on the detector energy resolution. The effects of these two factors, implantation depth and detector resolution, are illustrated in figures 9, 10 and 11.

Figure 9 shows simulations for implantation depths of 3, 5 and 10 μm for a detector of infinite energy resolution. When the implantation depth decreases, internal conversion and Auger electrons can escape from the detector, depositing only a small amount of energy in the implantation detector (note that electrons always deposit energy in the silicon detector). This effect becomes significant at an implantation depth of 3 μm. The different contributions to the top spectrum of Fig. 9 are detailed in Fig. 10. In this figure, we have displayed the spectra obtained considering only L, M or $N+$ conversion. Subsequent

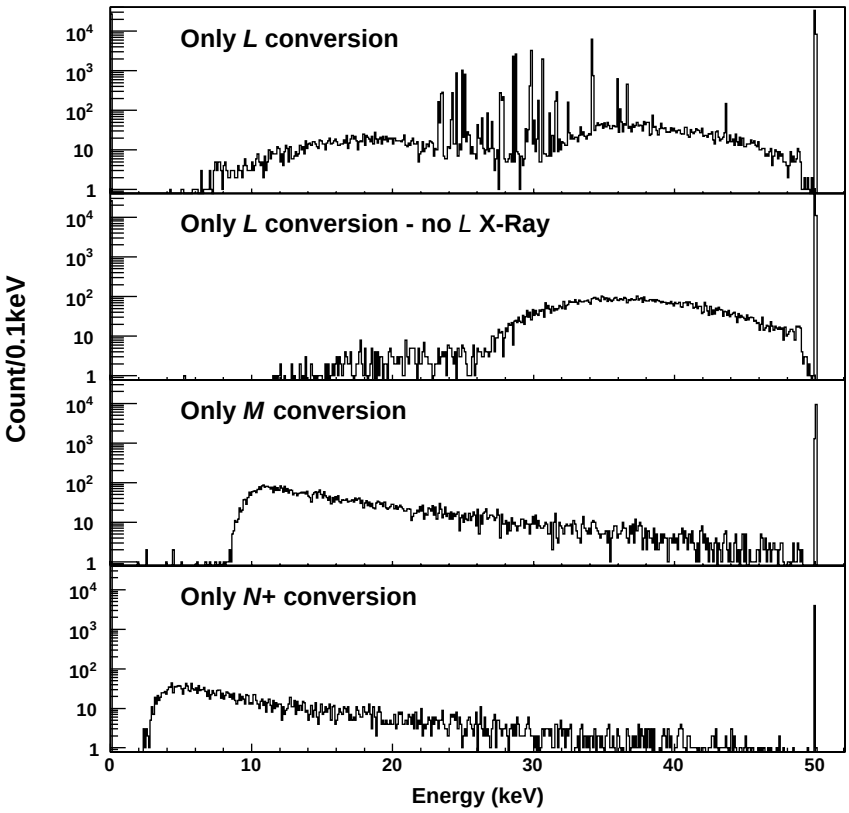

Fig. 10. Simulation for an implantation depth of 3 μm of different processes following the internal conversion of the 50 keV transition using the yields from this work. From top to bottom: i) Only L conversion is considered. Subsequent processes are included. ii) Same, but without L X-ray emission. iii) Only M conversion is considered. iv) Only $N+$ conversion is considered.

processes after the initial L, M or $N+$ vacancy are generated. We have also displayed the spectrum obtained after a L vacancy, but switching off the L X-ray emission.

In all panels of Fig. 9, the maximum of the deposited energy distribution is always at the full available energy, i.e. 50 keV corresponding mostly to pure electron cascades. As explained in the beginning of this section, the effective fluorescence yield ν_1 from the calculations presented in this work is smaller compared to that of Ref. [1]. Therefore, the probability of pure electron emission (i.e. no X-ray) is larger. Accordingly, the probability of full energy absorption is larger as shown in table 8.

Events for which all electrons are fully detected and an X-ray escapes from the silicon detector give rise to a deposited energy of 50 keV - E_X. These events are clearly visible in figures 9 and 10. The peak at 43.6 keV corresponds to

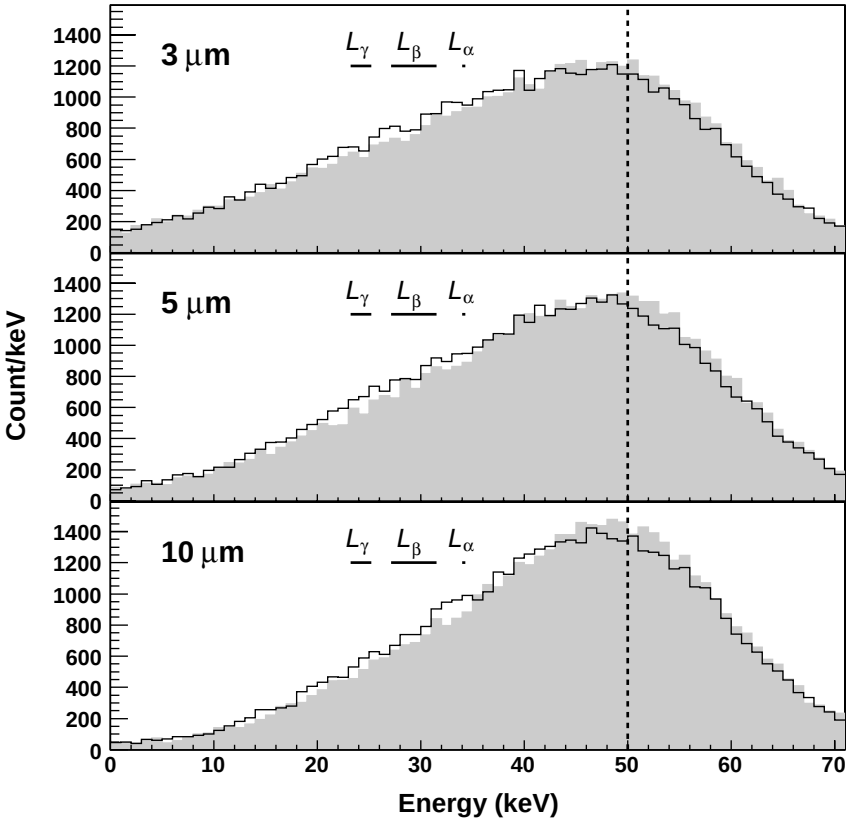

Fig. 11. Same as Fig. 9 with a detector resolution of 25 keV. Atomic yields are from this work (grey histogram) or from [2] (black curve).

Table 8
Characteristics of the simulated spectra for different implantation depths.

	Average energy (keV)		Fraction of full energy detected (%)	
Depth (μm)	Yields this work	Yields from [2]	Yields this work	Yields from [2]
3	39.6	38.8	56.0	52.1
5	41.8	40.9	63.9	59.0
10	43.8	43.0	70.1	65.7

the escape of a $L1$-$L3$ X-ray. The groups at ∼24 keV, ∼28 keV and ∼34 keV correspond to the escape of L X-rays with energies of ∼ 26 keV (L_γ group), ∼ 22 keV (L_β group) and ∼ 16 keV (L_α group), respectively. Note that L_α X-rays are emitted after $L3$ vacancy only. Since the effective $L3$ fluorescence yields from this work or from [2] are similar, one does not expect differences

around 34 keV except those due to the slightly different X-ray energies, at most 0.1 keV. The differences in the intensities expected in the L_γ and L_β groups are masked by the log scale of Fig. 9. Nevertheless, one can note the presence of an escape peak around 23.5 keV due to presence of the $L1$-O and $L2$-P X-ray lines around 26.5 keV, which are ignored in Ref. [2].
For an implantation depth of 10 μm, almost all electrons are fully absorbed in the Si detector. Differences between fluorescence yields are therefore enhanced compared to simulations performed at an implantation depth of 3 μm.
Figure 11 shows the simulated spectra convoluted with a detector resolution of 25 keV. Differences between the two simulations are, as expected, more pronounced for an implantation depth of 10 μm. Differences in intensity around 30 keV reflect the differences in effective ν_1 fluorescence yields. For smaller implantation depths, in particular at 3 μm, the difference around 30 keV is attenuated. Indeed, conversion and Auger electrons have a large probability to escape, leaving a fraction of their energy in the silicon detector: the probability to detect 50 keV - E_X is smaller. The difference in deposited energy is therefore spread over a larger energy range rendering the 2 distributions nearly identical. Note that this effect is not due to the X-ray detection efficiency which is almost the same as a function of the implantation depth: the probability for a 22 keV X-ray (L_β group) to deposit no energy in the silicon detector is 83.8% and 83.3% for a 3 μm and 10 μm implantation depth, respectively. Smaller fluorescence yields lead to two effects: i) a larger fraction of events with full energy deposition and ii) a smaller fraction of events with a deposited energy of 50 keV - E_X. Both effects lead to a larger average detected energy (see table 8).

We have also performed simulations for different implantation depths and a detector resolution of 40 keV. With this detector response, all effects are attenuated and differences due to the atomic yields are smoothed.
From all these consideration, large implantation depths help to discriminate between different atomic predictions, providing that a large statistics and good energy resolution are obtained. An infinite detector resolution would allow probing the fine structure as shown in Fig. 9; a finite detector resolution smooths the fine structure. Figure 12 shows simulations performed with a detector resolution of 15 keV, which can be achieved with state-of-the-art DSSD detectors. While the fine structure is still smoothed, the peaks corresponding to the X-rays escape and to the full absorption peak are resolved. A shown in table 8, the ratio between these two peaks can help to discriminate the different scenarios.
An implantation depth of more than 5 μm would be ideal to examine the differences in atomic yields but such a depth can only be obtained using inverse kinematics reactions. Furthermore, a drawback of large implantation depths is a degradation of the conversion-electron energy resolution and low-energy efficiency in the tunnel detectors due to the energy loss and absorption in the implantation detector.

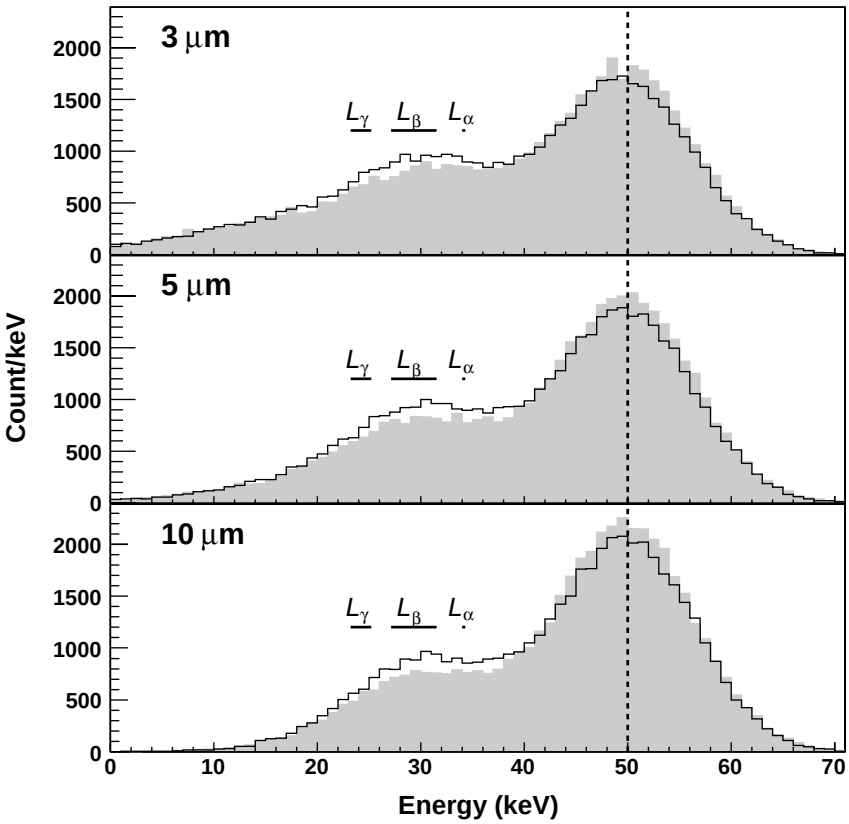

Fig. 12. Same as Fig. 10 with a detector resolution of 15 keV.

5 Conclusion

To conclude, the use of implantation detectors in heavy-element spectroscopy studies requires detailed calculations and simulations of atomic relaxation processes in order to interpret the fine structure of alpha-particle energy spectra. This is because the observed fine structure may not only be caused by the underlying physics: excitation energies, spins and parities of states in the daughter nucleus, which lead to different hindrance factors. Indeed, as shown in this work, the atomic processes involved in the electromagnetic decay of states in the daughter nucleus may also lead to an apparent alpha-particle fine structure. The distortions of alpha-particle energy spectra can be avoided by using other experimental techniques such as gas-jet transport systems. However, the price to pay is the loss of position correlations between the recoils and their daughter products.

New state-of-the-art atomic calculations show significant differences compared to Ref. [2]: large differences up to 50% are predicted for $L1$ fluorescence yields.

Experimental signals are however smoothed by the use of implantation detectors having a finite resolution, and by the summing of the different contributions following the electron conversion. A solution to overcome this problem and to remove the effect of implantation depth could be to measure X-ray fluorescence yields using a high precision low energy photon detector. The heavy actinide and transactinide elements are members of Mendeleev's periodic table for which atomic properties remain so far unexplored. High statistics experiments, using for example the high intensity stable beams of the Spiral2 driver (see *e.g.* [24]) coupled to high-resolution X-ray spectroscopy, could open new perspectives in this field.

References

[1] M.O. Krause, J. Phys. Chem. Ref. Data. 8 (1979) 307.

[2] R.B. Firestone, V.S. Shirley *et al.*, Table of isotopes, Eighth edition, John Wiley & sons, Inc, 1996.

[3] R. Jenkins, R. Manne, R. Robin and C. Senemaud, X-Ray spectrometry 20 (1991) 149.

[4] J. Bruneau, J. Phys. B 16 (1983) 4135.

[5] S.J. Rose, N.D.C. Pyper and I.P. Grant, J. Phys. B 11 (1978) 755.

[6] J.C. Slater, Quantum theory of molecules and solids, Mc Graw-Hill, New-York, Vol 4, 1974.

[7] C. Bonnelle and P. Motais, Phys. Rev. A 73 (2006) 042504.

[8] R.B. Firestone, private communication.

[9] A. Chatillon *et al.*, Eur. Phys. J. A 30 (2006) 397.

[10] R. Anne and A.C. Mueller, Nucl. Inst. Meth. B 70 (1992) 276.

[11] J. Simpson *et al.*, Acta Phys. Hung. N.S. - Heavy Ion Physics 11 (2000) 159.

[12] R.D. Page *et al.*, Nucl. Inst. Meth. B 204 (2003) 634.

[13] K. Hauschild *et al.*, Nucl. Inst. Meth. A 560 (2006) 388.

[14] S. Agostinelli *et al.*, Nucl. Inst. Meth. A 506 (2003) 250.

[15] R.S. Hager and E.C. Seltzer, Nucl. Data Tables A4 (1968) 1.

[16] E. Öz *et al.*, X-Ray Spectrom. 28 (1999) 198.

[17] M.S. Freedman, Ann. Rev. Nucl. Sci. 24 (1974) 209.

[18] M.S. Rapaport, F. Asaro and I. Perlman, Phys. Rev. C 11 (1975) 1740.

[19] M.S. Rapaport, F. Asaro and I. Perlman, Phys. Rev. C 11 (1975) 1746.

[20] O. Tarasov and D. Bazin, LISE++ code version 8.2.25. http://groups.nscl.msu.edu/lise

[21] J.F. Ziegler, SRIM-2006 code http://www.srim.org

[22] F. Hubert *et al.*, Atom. Dat. and Nucl. Dat. Tabl. 46 (1990) 1.

[23] L.C. Northcliffe and R.F. Schilling, Nucl. Data Tables A7 (1970) 233.

[24] M. Lewitowicz, Proceedings of the TOURS 2006 symposium on nuclear physics, AIP Conference Proceedings 891 (2007) 91.